ESA Climate Change Initiative – Fire_cci
D2.2 End to End ECV Uncertainty Budget (E3UB)

Project Name	ECV Fire Disturbance: Fire_cci
Contract Nº	4000126706/19/I-NB
Issue Date	30/04/2020
Version	1.1
Author	Joshua Lizundia-Loiola, Gonzalo Otón, Miguel Ángel Belenguer-Plomer, Mihai A. Tanase, M. Lucrecia Pettinari, Emilio Chuvieco
Document Ref.	Fire_cci_D2.2_E3UB_v1.1
Document type	Public

Project Partners

Prime Contractor/ Scientific Lead & Project Management	UAH – University of Alcala (Spain)
Earth Observation Team	UAH – University of Alcala (Spain) UPM – Universidad Politécnica de Madrid (Spain) CNR-IREA - National Research Council of Italy – Institute for Electromagnetic Sensing of the Environment (Italy)
System Engineering	BC – Brockmann Consult (Germany)
Climate Modelling Group	MPIM – Max Planck Institute for Meteorology (Germany) CNRS - Laboratory for Sciences of Climate and Environment (France)

Distribution

Affiliation	Name	Address	Copies
ESA	Simon Pinnock (ESA) Clément Albergel (ESA)	simon.pinnock@esa.int clement.albergel@esa.int	electronic copy
Project Team	Emilio Chuvieco (UAH) M. Lucrecia Pettinari (UAH) Joshua Lizundia (UAH) Gonzalo Otón (UAH) Mihai Tanase (UAH) Miguel Ángel Belenguer (UAH) Consuelo Gonzalo (UPM) Dionisio Rodríguez Esparragón (UPM) Ángel García Pedrero (UPM) Daniela Stroppiana (CNR) Mirco Boschetti (CNR) Thomas Storm (BC) Martin Böttcher (BC) Grit Kirches (BC) Angelika Heil (MPIM) Idir Bouarar (MPIM) Florent Mouillot (CNRS) Philippe Ciais (CNRS)	emilio.chuvieco@uah.es mlucrecia.pettinari@uah.es joshua.lizundia@uah.es gonzalo.oton@uah.es mihai.tanase@uah.es miguel.belenguer@uah.es consuelo.gonzalo@upm.es dionisio.rodriguez@ulpgc.es angelmario.garcia@upm.es stroppiana.d@irea.cnr.it boschetti.m@irea.cnr.it thomas.storm@brockmann-consult.de martin.boettcher@brockmann-cons... grit.kirches@brockmann-consult.de angelika.heil@mpimet.mpg.de idir.bouarar@mpimet.mpg.de florent.mouillot@cefe.cnrs.fr philippe.ciais@lsce.ipsl.fr	electronic copy

Summary

This End-to-End ECV Uncertainty Budget (E3UB) document describes the analyses that were made to identify and estimate the major sources of error that arise in each step of the Fire Disturbance ECV's final product retrieval process.

	Affiliation/Function	Name	Date
Prepared	UAH	Joshua Lizundia-Loiola Gonzalo Otón Miguel Ángel Belenguer Plomer Mihai A. Tanase	30/04/2020
Reviewed	UAH – Project Manager	M. Lucrecia Pettinari	30/04/2020
Authorized	UAH - Science Leader	Emilio Chuvieco	30/04/2020
Accepted	ESA - Technical Officer	Clément Albergel	05/05/2020

This document is not signed. It is provided as an electronic copy.

Document Status Sheet

Issue	Date	Details
1.0	30/03/2020	First Version of the document
1.1	30/04/2020	Addressing comments of Fire_cci+_D2.2_E3UB_v1.0_RID.doc

Document Change Record

Issue	Date	Request	Location	Details
1.1	30/04/2020	ESA	Section 2 Section 4 and sub-sections Section 4.3 Section 6	Small changes in the text Sub-sections reorganized, with the ones corresponding to FireCCILT20 and FireCCIS1S2AF10 merged and expanded. Text expanded. Additional references added.

Table of Contents

List of Tables

List of Figures

1   Executive Summary

The End-to-End ECV Uncertainty Budget (E3UB) document aims to identify and estimate the major sources of error that arise in each step of the ECV's final product retrieval process. In general terms, each step is related to a processing level. Those levels are typically known as Level-0, Level-1, Level-2, Level-3 (gridded data) and Level 4, although this naming convention has not been officially adopted by every space agency yet. This document tries to determine and estimate the distribution (uncertainty) that is followed by the errors that are caused by different effects throughout those levels, and provides a frame for their propagation. To do that, input sensors that were used by the different algorithms developed within the project for the burned area retrieval (Sentinel-1 SAR, Sentinel-2 MSI, Sentinel-3 Synergy, NOAA AVHRR, and Terra MODIS), and their corresponding ancillary data (Land Cover CCI, Active Fires, etc.) were properly characterised.

2   Introduction and objectives

Error characterisation and validation are critical phases to generate any Essential Climate Variable (ECV), and therefore both have an important role in the European Space Agency's (ESA) Climate Change Initiative (CCI) programme since its inception. While the validation gives information about the global quality of the product, the error characterisation tries to find out which factors are affecting those results and how they are distributed. This implies characterising every source of error and determining how they are propagated through the whole retrieval process, i.e. from the input data to the product estimates through the functions used to derive the estimates. The Guide to the Expression of Uncertainty in Measurement (GUM) that is maintained by the Joint Committee for Guides in Metrology (JCGM) describe this process as the "general law of error propagation" (GUM 2008).

It is important to separate two different stages in uncertainty characterisation that are clearly discernible in any Earth Observation (EO) data application. The first one encompassed the uncertainties of all processing levels that were applied prior to the usage of the EO data by the algorithm developer. In the case of burned area (BA) estimation, this refers to all the processes applied from raw data to generate the Level 1 (radiances) and Level 2 (reflectance) products. These processes occur before applying the BA algorithms, and therefore should be a responsibility of those in charge of the pre-processing algorithms. The second stage of uncertainty characterization deals with those factors related to the BA algorithm, which could be considered as the actual responsibility of the BA algorithm developers. They include all processes and transformations required to classify pixels as burned or not, as well as derived products (burned area estimates, for instance), which are offered to a higher level user. In the case of Fire_cci BA, this stage refers to the uncertainties associated to BA algorithms or any process used to produce the final pixel and grid products (see definition of both products in the Product Specification Document (PSD) of Fire_cci Phase 2 (Chuvieco et al., 2017) and its update in the Algorithm Development Plan (ADP) document (Pettinari et al., 2019)).

The definition of the previous two phases implies that the error characterisation of the first one needs to be based on existing literature, since it concerns several data providers of different processing levels (ground segments, space agencies, etc.) as well as different hardware and software (Mittaz et al., 2019). However, it is within the scope of the Fire_cci project to develop a proper uncertainty propagation framework for the second stage.

Uncertainty characterisation has been increasingly demanded for the last decades by different strata of the EO data user community and, hence, several attempts were done to provide an uninterrupted chain of error propagation at every processing level. For example,

in the case of the Moderate Resolution Imaging Spectroradiometer (MODIS) Level 1B product, the MODIS uncertainty index was developed by NASA to provide an estimation of the uncertainties related to that level (https://mcst.gsfc.nasa.gov/sites/default/files/file_attachments/M1054E_PUG_2017_0901_V6.2.2_Terra_V6.2.1_Aqua.pdf). For Sentinel data, Gorroño et al. (2017) designed a tool named Sentinel-2 Radiometric Uncertainty Tool (S2-RUT) that aims to estimate the radiometric uncertainty associated with each pixel in the Top-of-Atmosphere (TOA) reflectance factor images provided by ESA. In terms of ECV variables, the Sea Surface Temperature (SST) data producers within the CCI programme are making important progress in the uncertainty characterisation of the whole retrieval process by propagating the errors associated to Level 1 data of AVHRR to the final SST product (Merchant et al., 2017; Mittaz et al., 2019). Besides, different approaches (prognostic and diagnostic) for the characterisation of uncertainty in aerosol retrievals were recently reviewed by Sayer et al. (2019).

The antecedents on uncertainty quantification for BA products are limited. Giglio et al. (2010), for example, developed the BA uncertainty quantification used on the BA Global Fire Emissions Database version 3 (GFED3) and later on the version 4 (GFED4) products. The GFED products provide monthly aggregate BA extents at 0.25-0.5° spatial resolution based on the MCD64 BA product, which gives the date of detection at 0.5 km spatial resolution derived from MODIS imagery coupled with active fire observations of the same sensor (Giglio et al., 2009; Giglio et al., 2018a). The uncertainty of GFED products is expressed as a standard error of the BA extent estimated in the grid cell, and it is modelled with a linear regression of the burned patch residuals versus the actual extend of burned patches. In their study, the authors computed the per-patch residuals using reference data produced manually from Landsat imagery, at sample sites located in Siberia, Africa and North America.

Within the Fire_cci project three main analyses should be cited as precursors of the current document. Padilla and Chuvieco (2014) studied different general approaches that are used in error characterisation, although not all of them were found to be suitable for BA. They stated that the analytical based approach described in GUM 2008 could not be used in the Fire_cci project given the dependence of the products on complex spatiotemporal functions and decision trees. This is applicable to current Fire_cci algorithms since they detect BA using machine learning or spatiotemporal thresholding approaches, for which error propagation is considered unfeasible (Merchant et al., 2017). Similarly, the use of Monte Carlo simulations (Crosetto et al., 2001; Crosetto and Tarantola, 2001; GUM-101, 2008) to characterise the BA uncertainty was rejected by the authors. They considered that the input error simulations are frequently very complex, as they must emulate the autocorrelations between errors, which may vary in time and space. Furthermore, they stated that the Monte Carlo approach needs very large computational resources and the knowledge of the probabilistic distributions of the input data errors, which are not available in the Fire_cci data. Therefore, the authors used an inductive approach based on validation data and regression analysis, which was commonly used in land cover maps to analyse the probability of misclassification (Burnicki, 2011; Smith et al., 2003; van Oort et al., 2011).

The problem with this approach is that it was designed to provide a probability of burn only for the burned pixels and not, as it is required by definition and explicitly by the end-users, for both burned and the unburned classes, since every observed pixel has an associated uncertainty. A natural concern that also arises from these approaches is the quality of the sampling provided by such validation datasets, since even the larger and more systematic validation efforts may still provide only a limited sampling of the true uncertainties (Brennan et al., 2019).

Lewis et al., (2018) performed an assessment of the uncertainty estimates generated by several BA algorithms within the Fire_cci project, starting from the assumption that a per pixel estimate giving *the probability that a pixel should be labelled 'burned'* was provided. The actual aim of that assessment was to give some advice to algorithm developers about how to improve their uncertainty estimations, and also to show some examples on how the uncertainty was propagated through different processes such as BRDF or ratio of burn indices. Again, those propagation methods were more in line with the "general law of error propagation" described in GUM 2008, which, as was previously stated, it is not feasible to apply in the algorithms that have been and are being developed within the project. Conversely, the same document presented an approach to aggregate the uncertainty estimates from the pixel product to the climate modeller's 0.25-degree grid scale, which was acknowledged as valid for the current project (Section 5).

Finally, Brennan et al. (2019) estimated theoretical uncertainties for three widely used global satellite-derived BA products using a multiplicative triple collocation (TC) error model that was first described by Stoffelen (1998). This approach considers three observational records X_1, X_2, and X_3 of a variable with an unknown but true value T. The TC error model specifies that each observational record may be related to the truth via a linear measurement equation. The system can be solved based on three initial assumptions, i.e. each product has zero mean residual errors and the errors are uncorrelated with each other and with T. However, a requirement to apply this approach is that the three observation datasets explicitly cover the same temporal and spatial domain. Therefore, the three products were aggregated from the original pixel resolution products to a common sinusoidal grid with a spatial resolution of 1° at the Equator in 16-days periods, which may imply new sources of uncertainty. Obviously, this approach cannot be used in the Fire_cci project since it needs three different BA products to obtain what is called the 'true' value.

Taking all this into account, three main objectives or steps were established for the current deliverable:

1. Provide a detailed overview of what is available in the literature about error sources, uncertainty characterisation and propagation in the pre-processing phase: those processes required to obtain the input data for each BA algorithm developed within the Fire_cci project. In that sense, we will follow the guidelines of Mittaz et al. (2019), which show how to apply the principles of metrology to deal with those issues in EO.

2. Design an uncertainty characterisation and propagation framework for the BA algorithms. In the case of threshold-based algorithms the idea, whenever possible, is to use validation data along with Monte Carlo simulations based on the knowledge of the error's correlation and distribution obtained in the previous step 1. For those algorithms that use machine learning approaches a simple way of characterizing uncertainty is to use the classification probability, which describes the likelihood that a pixel belongs to the burned class.

3. Provide an aggregation methodology to propagate the uncertainty from the pixel to the grid product. To do that, the approach proposed by Lewis et al. (2018) will be used.

As a result, and similarly to the previous Fire_cci projects, an important practical output of the error characterisation called uncertainty layer will be generated for the pixel and grid product. For the pixel product, the uncertainty will be expressed in probabilistic terms, as the probability that a pixel is really burned. This layer was named confidence level in the

previous version of the Fire_cci products (Chuvieco et al., 2017). For the grid product, uncertainty will be expressed as a standard error of the total burned area for each grid cell, as requested by the Climate Research Group (CRG) (Chuvieco et al., 2017).

3 Uncertainty characterisation through pre-processing steps

3.1 General overview

In a laboratory the uncertainty is characterised by the statistical evaluation of repeated measurements. In EO this is not possible due to the variation in sensor state, viewing geometry, and natural geophysical variability. Besides, the atmosphere modifies the TOA radiance observable from space by processes of scattering, absorption, and emission. The impact of the atmosphere in the radiance depends on the vertical profile of radiatively-active gases, aerosols and clouds. Surface changes caused by variations in moisture, temperature, or vegetation phenology, among other factors. These variations also affect reflected radiance and may confuse the detection of actual cover changes, such as those caused by fire disturbances.

To understand the uncertainty propagation throughout the process of measurement and posterior transformations of the obtained data a key term is the level of processing of an EO product. Processing levels reflect both distinct computational stages in handling data streams downlinked from satellites and the different institutional arrangements for creating products at different levels (Mittaz et al., 2019). Although it is not yet standardized among agencies and communities that provide those products, typically five levels can be differentiated:

- Level 0 (L0): This level includes the raw telemetry that is downlinked by a ground receiving station, which comprises a mix of scientific observations together with engineering data. Transforming L0 data to scientifically useful products is complex. One of the main sources of uncertainty is the digitisation carried out to transform the analogic signal into digital. The raw sensor data is binary (10 to 16 bits), but such digitisation is coarse compared to laboratory metrology. That binary representation of the raw sensor values places a fundamental lower limit on the uncertainty present in the calibrated radiances. For example, 10-bit digitisation corresponds to 0.1% resolution of the range (Mittaz et al., 2019). In addition to this source, L0 processing involves estimating the satellite orbit and the origin of the measured radiances projected onto Earth's surface (known as geo-locating). In this case the uncertainty increases depending on the quality of the orbit information, i.e. if it is Near Real Time (NRT) or Non-Time-Critical (NTC) improved geo-location.
- Level 1 (L1): It includes calibration parameters to map the counts into radiance and the derived calibrated radiances. Auxiliary data locate the radiances in time, latitude, and longitude and provide information related to satellite and solar zenith and azimuth angles. At this level the main sources of error are the calibration parameters (gain and offset) that are part of the measurement function. In this case, this function allows the previously mentioned mapping of counts into radiance. Changes in those parameters are to be expected as the sensor's space environment changes and the sensor degrades. This means that the uncertainties associated with measured radiances will evolve. Typically, after 3-10 years a sensor will fail or will be decommissioned. In the case of multi-decadal datasets, the sensors are supposed to have identical spectral response but they have significant differences in their Spectral Response Function (SRF).
- Level 2 (L2): This level normally involves the inverse estimation from radiances of one or more geophysical variables. The retrieval algorithms used in EO for that

purpose are highly varied. As in previous levels no uncertainty information is included at this level. Users of L2 often interrogate pixel level quality indicators for indications, but quality indicators change from one product to another. In that sense in ESA CCI they reached a consensus with regards to best practice for geophysical products (Merchant et al., 2017).

- Level 3 (L3): They are gridded products, made by aggregating L2 values in space and/or time on a regular space-time grid. Therefore, it implies averaging the L2 (sometimes weighted). Assuming the sampling or the aggregation is independent from the variability, the resulting sampling error has an expectation of zero. But the error distribution has a width that is not negligible compared to the uncertainty of the value.

- Level 4 (L4): It typically includes complete gridded gap-free in space and time information, which in many cases involves interpolation, and hence, a specific error propagation.

Officially, none of the previous levels have an uncertainty characterisation included and no complete traceable analysis and propagation of uncertainty from L0 to L4 exists (Mittaz et al., 2019). This means that algorithm developers have no chance to include as input the error characterisation of previous levels and, therefore, to generate a proper error characterisation of their own processes. The following sub-sections try to characterise from existing literature the different error sources of those previous levels to somehow show the diversity and nature of the errors that should be taken into account.

3.2 Terra-MODIS Level 2G

Three products are used as main inputs for the FireCCI51 algorithm (Lizundia-Loiola et al., 2020) related to the Terra satellite's MODIS sensor: the MOD09GQ product, which provides an estimate of Red and Near-Infrared (NIR) surface reflectance at 250 m spatial resolution, the MOD09GA product, which provides, along with the rest of the reflectance and emissive bands, the state QA flags used by the algorithm at 1000 m spatial resolution, and the MCD14ML active fire product. This latter product includes also Aqua satellite data and will be covered in the ancillary data section (Section 3.7), as it is only used for guiding the training phase.

Four MODIS processing levels are differentiated based on the MOD09 user guide (Vermote et al., 2015). L0 data is raw satellite data that feeds L1 data that has been radiometrically calibrated, but not otherwise altered. L2 data is L1 data that has been atmospherically corrected to yield a surface reflectance product. L3 data is L2 data that has been gridded into a map projection, and usually has also been temporally composited or averaged. L4 data are products that have been put through additional processing. All data up to and including L2 are in an ungridded orbital swath format, with each swath typically cut into small segments, or granules, to facilitate processing. Data at L3 and up are geo-located into a specific map projection, with the geo-located products typically in a set of non-overlapping tiles. The L2G-lite format, consisting of gridded L2 data, was developed as a means of separating geo-locating from compositing and averaging.

Several scientific teams are responsible for the quality of the MODIS products. The MODIS Land Quality-Assessment team, for example, evaluates and documents the scientific quality of the MODLAND products with respect to their intended performance. The MODIS Characterization and Support Team (MCST) is responsible for developing and maintaining the MODIS calibration product (L1B algorithm), which is a precursor to every geophysical science product. In this last case, there has been an attempt to characterise the uncertainty that affects the L1B creation process through the inclusion of

uncertainty data on a pixel-by-pixel basis. The reflective solar bands uncertainty algorithm is based on characterization of the Earth View (EV) scene reflectance (Xiong et al., 2013). To compute it, the uncertainty of the Solar Diffuser/Solar Diffuser Stability Monitor calibration, the lunar calibration, EV response trending, the temperature correction and the scene dependent instrument noise are taken into account.

In the following step the L1B is corrected for the effects of atmospheric gases and aerosols to obtain the L2 product (MOD09). Thus, an estimate of the surface spectral reflectance for each band as it would be measured at top of canopy if there were no atmospheric scattering or absorption is obtained. Band quality control information for the correction is also generated (e.g., flags denoting if ancillary data is unavailable, if L1B data is faulty, etc.). However, this layer does not represent actual uncertainty propagation data, but a general band quality of the Atmospheric Correction (AC).

Finally, daily MOD09 L2 data is aggregated in standard MODIS sinusoidal tiles (MOD09GA and MOD09GQ L2G-lite). The number of daily observations at each pixel is determined not only by the number of orbits at that location (one at the equator and up to 15 at the poles), but also by the spread of observational coverage of off-nadir pixels. After identifying all the observational values for each location, the most suitable reflectance value is selected for each pixel based on observational coverage and view angle, and whether the observation is flagged as cloudy, clear, containing high aerosol or low aerosol, or cloud shadow.

The L2G-lite products, which are the inputs for FireCCI51, include a layer of the band quality that cannot be considered a proper uncertainty layer. Although the original uncertainty of the L1B product is somehow taken into account when setting the quality of a pixel, it provides qualitative information instead of a quantitative description of how errors are propagated and distributed. No information is officially provided in the products regarding the error propagation through the AC, projection of the data or how the ranking that is used to select the best observation affects uncertainty.

In that sense, Vermote et al (2008) made an estimation of the sensitivity of surface reflectance to uncertainties in input key atmospheric parameters using a theoretical error budget. Such a budget was created based on the simulation of a number of atmospheric and geometrical scenarios (Vermote and Saleous, 2006). In that study, uncertainties from the instrument calibration (±2%), atmospheric pressure (±10 mb), water vapour content (±0.2 g/cm^2), ozone content (±0.02 cm·atm), retrieved Atmospheric Optical Thickness (AOT) values (resulted from the aerosol inversion), and selection of the aerosol model (urban polluted, smoke low absorption, smoke high absorption, or urban clean) were considered. They found that the overall accuracy of surface reflectance varies in dependence of the band and AOT. Under clear atmospheric conditions they stated that it does not exceed 0.006 in reflectance unit. The MODIS product theoretical uncertainty bars were set to 0.005+0.05ρ for the surface reflectance under favourable conditions (no high aerosol). To check the quality of the MOD09 they analysed a year of Terra data (2003) collected over 150 AERONET sites. The results showed that the average percentage of observations that lay within the theoretical uncertainty for bands 1 (645 nm), 2 (870nm), 3 (470 nm), 4 (550 nm), 5 (1240 nm), 6 (1650 nm), and 7 (2130 nm) was equal to 88.66%, 94.34%, 50.52%, 79.34%, 96.50%, 97.87%, and 98.62%, respectively. The band 2 NIR, which is used by the FireCCI51, showed one of the highest proportions of "good" observations.

Regarding the state information that is used from the MOD09GA, although it is unclear the origin of all bit values included on it, it seems that the main source is the MOD35 developed by the MODIS Cloud Mask Team (Ackerman et al., 2010). This product, which is based

on L1B radiance data, assumes that its inputs are calibrated and quality controlled and no propagation of its uncertainties is made. In the process of identifying pixels, several thresholds are used and hence, as one approaches the threshold limits, the certainty or confidence in the labelling becomes more and more uncertain. For that reason, a confidence layer is provided that tries to be an alternative to uncertainty considering it as a function of how close the observation is to the thresholds.

3.3   Sentinel 3-Synergy Level 2

This product is the input for the FireCCIS310 algorithm, which will be available for the years 2019 and 2020. One unique product is used as main input related to the Sentinel-3 (S3) satellite's OLCI and SLSTR sensors: the SY_2_SYN product, which provides an estimate of Visible, NIR and Short Wave Infrared (SWIR) surface reflectance at 300 m resolution, along with the rest of the information, e.g. quality flags or geometry.

Several processing levels, similar to those established by MODIS, can be differentiated based on the S3 OLCI, S3 SLSTR and S3 Synergy (SYN) Product User Guides (PUG, https://sentinel.esa.int/web/sentinel/user-guides, last accessed February 2020). L0 data is raw satellite data that includes time sorted and annotated data from Instrument Source Packet (ISP). These data, the orbit scenario file and several auxiliary data files feed the L1 EO processing chain. The derived product is called L1B and provides radiometrically calibrated, geo-referenced and annotated radiances. These first two levels are common but independent for both OLCI and SLSTR sensors and, hence, two L1B products are obtained, respectively. In the following step, these two products are used to feed and generate the internal SYN L1 product (SY_1_MISR). This process aims to project all OLCI and SLSTR bands on the same SYN reference grid (i.e. the OLCI acquisition grid), using the inter-instrumental misregistration estimated for both sensors' bands. Finally, in L2 that internal information is atmospherically corrected to generate surface directional reflectances stored in the SY_2_SYN product. As in the case of MODIS, all data up to and including L2 are in an ungridded orbital swath format, with each swath typically cut into small segments, or granules, to facilitate processing. However, in the case of SYN there is not any processing level equivalent to the L2G-lite of MODIS. Therefore, SYN L2 information is aggregated into daily non-overlapping tiles of 10x10 degrees by Brockmann Consult (BC) for internal use.

The quality of the S3 products is responsibility of the full Ground Segment and mainly of the Payload Data Ground Segment (PDGS). It operationally generates the user products and distributes L0 raw products, processed L1 products and derived L2 products. However, there is no official uncertainty propagation process integrated through the different levels.

In the case of the OLCI L1B products only quality flag information (saturated radiances, dubious locations, where cosmetic was applied, bright pixels, sun glint risk, etc.) is provided within the product (ACRI-ST IPF Team, 2017), along with some information related to the observation environment, such as the geometry tie points and meteorological tie points. It is supposed that an error estimate band of the radiance is included, but no such layer was found in the downloaded data from the open hub (https://scihub.copernicus.eu/dhus/#/home, last accessed March 2020). A similar approach is followed for SLSTR, although in this case the previous information is extended due to the availability of SWIR and Thermal Infrared bands (ACRI-ST IPF Team, 2018). Each SLSTR band is provided along with a quality data layer that contain estimates of the random signal noise per scan line derived from the on-board calibration sources (the VISCAL and the blackbodies), and

correlated radiometric uncertainties as a function of scene radiance or/and brightness temperature (BT) derived from the pre-launch calibration.

Although there is no proper uncertainty propagation information within the official products, some attempts to assess the per pixel uncertainty of both sensors L1B products have been found in the literature.

On the one hand, Hunt and Nieke (2016) developed a software tool to determine the per pixel uncertainty of the OLCI L1B images. It was developed following the approach outlined in GUM (2008) and was created with the goal of integrating it in the S3 Toolbox (now called Sentinels Application Platform, SNAP) software package as a plugin. Similarly to Mittaz et al. 2019, they first describe the OLCI measurement model of the L1B radiances to characterise the contributors of the overall uncertainty model. Then, they defined an uncertainty model as a function of the total signal (noise), radiometric calibration (diffuser BRDF estimated at 0.3%, diffuser alignment estimated at 0.31%, diffuser aging, calibration diffuser stray light estimated at 0.08%, calibration camera stray light estimated at 0.2% and calibration speckle estimate at typically 0.1%), non-linearity (CCD and ADC non-linearity), dark signal (offset compensation and dark stability error), smear (smear gain contributions) and stray light contribution. Hunt and Nieke (2016) showed uncertainties around 0.76% for a specific preliminary example for a region in Northern Sahara.

On the other hand, Etxaluze and Smith (2019) have recently developed a tool called MapnoiS3 to allow users of SLSTR L1B data to derive per pixel uncertainty estimates for both radiance and thermal channels using the information contained in the L1B product and additional auxiliary data files (ADF). Using the random signal noise and correlated radiometric uncertainties included in the quality layers they are able to generate a new NetCDF file where the scene radiance/BT uncertainty, noise equivalent radiance/BT and, in the case of BT, the partial derivative of the radiance as a function of temperature are included. The contributors to the total uncertainty slightly differ from radiance to BT. In the first case, the total radiometric noise is considered to be composed of the noise related to the light intensity level (shot noise) and the electronic noise (dark current, amplifier noise, reset noise, digitisation). However, Etxaluze and Smith (2019) stated that at the high-level quantisation of SLSTR the digitisation, amplifier and reset noise are insignificant. In the latter case, the radiometric noise is considered to be composed of the noise equivalent differential temperature per scan line.

In the following processing steps, regarding the SYN product, two consecutive products are generated: the L1C and the L2. The former is only for internal use and it is not resampled to a specific surface grid or projection but includes all the necessary misregistration information so that any user-defined projection or gridding can be performed at a higher level (S3 Team, 2011). There is not any mention to the uncertainty in the whole L1C Algorithm Theoretical Basis Document (ATBD). The latter contains atmospherically corrected surface directional reflectance referenced at OLCI geometry that is generated based on the L1C product. However, in this case there is a dedicated section to the retrieval error estimate of the L2 product (North and Heckel, 2010). Two main contributors are analysed there: the error in Aerosol Optical Depth (AOD) and the surface reflectance error as a function of the previous error, sensor noise and estimated error in the radiative transfer model. This last error is computed for each spectral band and included as a separate layer along with the reflectance layer. It is offered in the same relative units of reflectance (%). Since the ATBD was published previous to the development of the above mentioned L1B uncertainty tools, there is not any mention to them. The lack of official

error distribution characterisation at previous levels along with the lack of information of that process questioned the reliability of those layers. However, we consider the inclusion of a per pixel uncertainty layer a great improvement and its use will be studied.

In the last step, the SY_2_SYN L2 product is aggregated temporally into daily images and spatially into 10x10 degree tiles. The scientific content of the product is not in any case altered, but the best observation is selected when more than one valid observation is available for the same pixel. Similarly to what is done with the MODIS L2G lite product, the best observation is considered when OLCI zenith angle (OZA) is minimum. The values of all the layers of the selected image are kept in the final aggregated daily product including the uncertainty associated to that pixel.

3.4   NOAA-AVHRR LTDR Level 2G

FireCCILT10 (Otón et al., 2019) uses the AVH09 Surface Reflectance Product (Version 5) that is provided by the Land Long Term Data Record (LTDR, Pedelty et al., 2007) project. It is based on the Global Area Coverage (GAC, 4x4 km) data with a final spatial resolution of 0.05º degree (≈5 km). AVH09 covers four decades (1981–present) and it includes up to two sensors (AVHRR2 and 3) on board seven different NOAA satellites (7, 9, 11, 14, 16, 18, 19). It provides Red and NIR Surface Reflectance, and TOA BT, all of them used by the FireCCILT10 algorithm.

First, L0 data is converted on AVHRR L1B (Robel et al., 2014), which contains the main geophysical parameter reflectivity (for channels 1, 2 and 3a) and calibrated radiances (for channels 3, 4 and 5) (EUMESAT, 2011). At this point, the uncertainty is affected by several features, such as the Platinum Resistance Thermometer (PRT) noise and bias, earthshine, Temperature gradient, PRT representation, detector noise, digitisation, amplifier, SRF, time mismatch, space mismatch, azimuthal asymmetry, solar contamination, pre-flight characterisation, degradation and instrument temperature dependence. Some of these sources directly affect thermal gradients across the internal calibration target and the estimation of calibration parameters. Regarding the solar reflective bands, the calibration is different for the visible and the infrared (IR) channels (EUMESAT, 2011). Although Red and NIR bands are calibrated prior to launch (Robel et al., 2014), the calibration is applied to the data afterward with linear decay because there is not effective on-board calibration (Holben et al., 1990). The uncertainty in the calibration is estimated to be of the order of 5% (Robel et al., 2014). In the case of the emissive bands, BT is calibrated in flight with an uncertainty estimated at ±0.1 K (Trischenko et al., 2002). In both cases several problems were observed due to the combination of different sensors and satellites. In general, AVHRR3 was seemed to have better radiometer consistency than AVHRR2 (Trischenko et al., 2002). Besides, it was observed that the calibration of the different satellites generated a range of variability in the measurements that, in the case of BT, could be more than 0.5 K (Trischenko et al., 2002; Mittaz et al., 2019). A quality decrease and a systematic degradation of the radiometric sensitivity as a function of time and launch processes was observed as well. This degradation was quantified in ≈1-3% per year by Uprety et al. (2011) in the case of the solar reflective bands and below 1% in the case of BT. These generates a reduction in radiometric resolution over time and, in the case of BT, expands the upper limit of the measured BT. In any case, a proper characterisation of the uncertainty generated by all those sources cannot be done since there is not access to the pre-launch measurements and to the original manufacturer's data propagation (Mittaz et al., 2019).

In the following step, L1B is transformed in GAC, reducing in real time the spatial resolution of the acquired image (EUMESAT, 2011). Four out of every five samples along the scan line are used to compute one average value, and the data from only every third scan line are processed. As a result, the spatial resolution of GAC data near the subpoint is 1.1 km by 4.4 km with a 2.2 km gap between pixels across the scan line (Robel et al., 2014; EUMESAT, 2011). Bulgin et al. (2016) estimated the uncertainty of this averaging process on about 0.04 K.

Finally, GAC is processed to obtain AVH09 L2G product, after applying some improvements. These improvements include: radiometric in-flight vicarious calibration for the visible and near infrared channels, inverse navigation to relate an Earth location to each sensor IFOV, atmospheric corrections for Rayleigh scattering, ozone, and water vapour, aerosol correction, and BRDF corrections used in MODIS processing (El Saleous et al., 2000; Pedelty et al., 2007). Calibration is a critical issue for applications using multiple sensors, including multi-decadal data analysis (Mittaz et al., 2019), and AVH09 has demonstrated 1% calibration accuracy for the visible/NIR bands (Pedelty et al., 2007). However, an uncertainty characterisation and propagation through the above mentioned processing levels is still needed.

3.5   Sentinel 2-MSI Level 2

The Sentinel-2 (S2) MSI L2 processing chain generates, using as input the TOA L1C orthoimagery, Bottom-Of-Atmosphere (BOA) corrected reflectance orthoimages. Additionally, an AOT map, a Water Vapour (WV) map and a Scene Classification Map (SCM) together with Quality Indicators (QI) for cloud and snow probabilities are generated. S2 bands at 10, 20 and 60 m spatial resolution are required for L2 processing. Spectral bands 2, 3, 4, 8 (Table 1) as well as a True Colour Image (TCI) and AOT and WV maps are provided at 10 m. Spectral bands 2-7, 8A, 11, and 12, and resampled TCI, AOT and WV are provided at 20 m. Band B8 is omitted as B8A provides more precise spectral information. All components of the 20 m product are resampled to 60 m as well. The cirrus band 10 is omitted, as it does not contain surface information.

Table 1. Central wavelength (nm) of each band of the MSI aboard Sentinel-2 A and B.

Satellite	B02	B03	B04	B05	B06	B07	B8A	B11	B12
S2A	492.4	559.8	664.6	704.1	740.5	782.8	864.7	1613.7	2202.4
S2B	492.1	559.0	665.0	703.8	739.1	779.7	864.0	1610.4	2185.7

The Sen2Cor (Main-Knorn et al., 2017) processor is a combination of state-of-the-art techniques for performing atmospheric as well as topographic corrections which have been tailored to the S2 environment together with a scene classification module. The scene classification algorithm allows detection of clouds, snow and cloud shadows and generates a map which contains three different classes for clouds (including cirrus) together with six additional classes: shadows, cloud shadows, vegetated, not vegetated, water and snow. Such a classification is an important information source for uncertainty as it may be used to mask out the pixels covered by clouds and its shadows and then not classify them. However, such a classification also has intrinsic uncertainty related which should be considered. The Shuttle Radar Topography Mission Digital Elevation Model (SRTM DEM) is also used when pre-processing the S2 data. The SRTM DEM has vertical errors between 4-6 m (Goncalves and Fernandes 2005). Such errors may increase the uncertainty when mapping BA, especially over steep slopes.

Finally, BA mapping uses datasets acquired by different satellites (S2 A and B), which may generate geolocation errors. Thus, it is expected that any geolocation error may be significant at fire borders.

3.6 Sentinel 1-SAR

Sentinel-1 (S1) is a two-satellite constellation (A - since April 2014, B - since April 2016) to provide C-Band SAR data continuity following the end of ERS-2 and Envisat missions. The satellites carry a C-band SAR sensor, which offers medium and high-resolution imaging in all weather conditions making it useful for land monitoring. The radar instrument may acquire data in four modes, with the Interferometric Wide (IW) swath (250 km width) being the default operation mode over land. The IW mode images three sub-swathes using the Terrain Observation with Progressive Scans SAR (TOPSAR) to provide high quality, homogeneous images. The advantages of S1 sensor over other C-band SAR missions, besides the free data access policy, are three-fold, i) high temporal frequency (6 days exact repeat cycle with two satellites), ii) high spatial resolution (5 m in azimuth and 20 m in range) and, iii) dual-polarization (VV and VH). One should notice that nominal temporal frequency is not yet achieved over areas outside Europe and North America and that areas with frequent seismic activity (e.g., the Andes) are imaged in single polarization mode (VV) for increased spatial resolution. S1 products are released in two L1 formats, Ground Range Detected (GRD) and Single Look Complex (SLC). GRD products are projected, intensity images, radiometrically and terrain corrected. SLC data are designed for interferometric applications, containing both phase and intensity information. The most commonly available SLC and GRD data are acquired in IW mode. L1 GRD data multi-looked and projected to ground range using an Earth ellipsoid model (typical product size is 1GB for dual-pol IW mode) is considered to map BA.

Speckle appears as a granular interference that inherently exists in coherent image systems as the SARs. The presence of speckle makes SAR imagery very different from optical datasets. As the scatterers are not identical for each cell, the signal fluctuates due to its high sensitivity to small variations in scatterers' relative location and properties. Differences in the magnitude of the signal intensity between two dates may appear due to fire unrelated changes (e.g. changes in relative position of the scattering elements within a resolution cell due to wind) which influences uncertainty. To meet the accuracy requirements of most SAR-based applications, a large equivalent number of looks (ENL) is often used, with values around 100 being typically advised (Quegan et al., 2001). ENL describes the degree of averaging applied to the SAR measurements during data formation and post-processing (Anfinsen et al., 2009). The usual approach to reduce speckle is filtering in the spatial domain. When multiple intensity images of a scene are available (repeat passes), an attractive way to increase the ENL is by linearly combining the images (multi-temporal filtering). Previous experiments, carried out within Fire_cci Phase 2 Option 3, showed small differences (~4) in ENL between S1 products processed with increasing multi-look factors, i.e., spatial spacing of 20, 30, and 50m. At the same time, Sentinel-1 products showed a significantly larger ENL when combining spatial (multi-looking) and temporal filtering. Spatial aggregation to 40 m (2x10 looks) followed by multi-temporal filtering provided ENL values around 80. Moreover, the SAR instruments aboard of S1-A and B satellites have a radiometric error of 0.38 and 0.36 dB, respectively (Schwerdt et al., 2017). We expect that data uncertainty will have low relevance in the results according to previous studies (Belenguer-Plomer et al., 2018).

Apart from intrinsic sensor-related uncertainty (e.g. absolute calibration) environmental conditions at SAR image acquisition may influence BA detection and mapping. Changes

in soil moisture may increase BA detection and mapping uncertainty as it may entirely mask out fire-induced variations of the backscatter coefficient or result in fire unrelated backscatter changes (Belenguer-Plomer et al., 2019). However, such effects cannot be measured with precision since current global soil moisture products have a much coarser spatial resolution than S1 data. Topography also introduces uncertainty when using SAR-based datasets as the SAR backscatter coefficient is modulated by terrain slope thus conditioning the accuracy of BA detection (Kalogirou et al., 2014; Kurum, 2015).

3.7 Ancillary data

Two main ancillary data are used by the different algorithms that are being developed within the Fire_cci project: thermal anomalies and land cover information. Both products are high level products (L3 and L4, respectively), which means that they are based on the above mentioned processing levels that do not include proper uncertainty characterisation.

3.7.1 Terra and Aqua MODIS active fires

The first source of thermal anomalies that is used by some of the algorithms developed within the project is the MODIS MCD14ML collection 6 product.

In the case of MODIS, the most basic fire products in which active fires and other thermal anomalies (such as volcanoes) are identified are the MOD14 product based on Terra satellite's MODIS and MYD14 based on Aqua satellite's MODIS (Giglio et al., 2018b). These L2 products are defined in the MODIS orbit geometry covering an area of approximately 2340×2030 km in the along-scan and along-track directions, respectively. Regarding the uncertainty characterisation of the active fires, a detection confidence level is provided, which intended to help users gauge the quality of individual fire pixels. This confidence estimates ranges between 0% and 100% and is used to assign one of the three fire classes (low-confidence fire, nominal-confidence fire, or high-confidence fire) to all fire pixels (Gilgio et al., 2018b). The confidence of each detected fire pixel is calculated as the geometric mean of up to five sub-confidence parameters that are defined in terms of the temperature, the number of adjacent water pixels, the number of adjacent cloud pixels and two standardised variables (Giglio et al., 2016). All the parameters used for the detection are related to the algorithm used to detect thermal anomalies and the uncertainties of the previous processing levels are not taken into account. Besides, no confidence level information is provided for those pixels that were non-detected as fire or filtered in the processing. Thus, this confidence level can only be used as an approximation of the product uncertainty.

The level 3 MCD14ML product is generated based on MOD14 and MYD14. This monthly fire location product contains the geographic location, date, and some additional information for each fire pixel detected by the Terra and Aqua MODIS sensors on a monthly basis. The product is distributed as a plain ASCII (text) file with fixed-width fields delimited with spaces. One of its attributes is the previously mentioned confidence level.

3.7.2 NOAA-20 and SUOMI-NPP VIIRS active fires

Information related to the VIIRS products is significantly lower than for the MODIS ones. VIIRS products are supposed to continue with the MODIS time series so most of the algorithms are being adapted to the new sensor. Therefore, the conclusions reached for MODIS active fires in the previous section (Section 3.7.1) can be considered as the best scenario for VIIRS active fire uncertainty characterisation.

Currently there are two satellites providing active fire products based on VIIRS: the Suomi-NPP and the NOAA-20 (JPSS-1). Recently, the Fire Information for Resource Management System, FIRMS (https://firms.modaps.eosdis.nasa.gov/, last accessed March 2020) has included an option to download separately NRT active fires from Suomi-NPP and JPSS-1, although it is supposed that in both cases the algorithm described in Schroeder et al. (2014) is applied. At NTC level, a first collection of two L3 products called VNP14ML (750m) and VNP14IMGML (375 m) are currently being produced, although it seems that only Suomi-NPP detections are included. In those products the % confidence level has been replaced by confidence classes (low, nominal, and high).

3.7.3 Land Cover CCI

In the previous Fire_cci phases the source of the Land Cover information was the ESA CCI Land Cover (LC) project. That project produced annual LC maps since 1992 until 2015. More recently, this dataset has been extended within the Copernicus Climate Change Service (C3S) to the years 2016-2019 allowing users to have global and annual updated LC information at 300 m resolution. The algorithms used in both cases are equal so the consistency of the dataset is ensured (ESA, 2017a). Regarding uncertainty characterisation, there is not such information included in the dataset, although hard work has been done to determine the quality (validation) of the product (ESA, 2017b).

## 4 Uncertainty characterisation through BA algorithms

Taking into account the current situation of the uncertainty characterisation in the products that are used as input in the Fire_cci project algorithms, a proper characterisation and propagation of the input uncertainties through the algorithms is not feasible. Not only because the different algorithm structures prevent a mathematical propagation through themselves, but also because of the inexistence of such input data. However, an effort is being carried out to analyse how the uncertainty approximations described in the previous section (Section 3) can be used to somehow assess the impact of the algorithms in the final results.

4.1 FireCCI51

Regarding this product there are not any changes expected since the current project will extent the existing time series from 2001-2017 to 2001-2019. Logistic regression analysis was used following a k-Fold validation (k = 10) to estimate BA probability as a surrogate of uncertainty characterization of the BA algorithm. The model was trained from 10 calibration sites, which encompass a wide range of different vegetation and fire patterns, using data from 2008. Four input variables were included in the logistic models: monthly NIR composite (NIR), monthly relative NIR drop (RelΔNIR), distance to the nearest BA seed (distance), and number of valid observations in the first 10 post-fire days (obs) (Lizundia-Loiola et al., 2018). The final coefficients derived from the logistic regression analysis were:

$$pB = \frac{1}{1 + e^c}$$

Where pB is the BA probability and $c = -(3.533 - 0.01175 * obs - 0.001996 * NIR + 0.01417 * Rel\Delta NIR - 0.0009282 * distance)$. An example of an area of Northern Australia is shown in Figure 1.
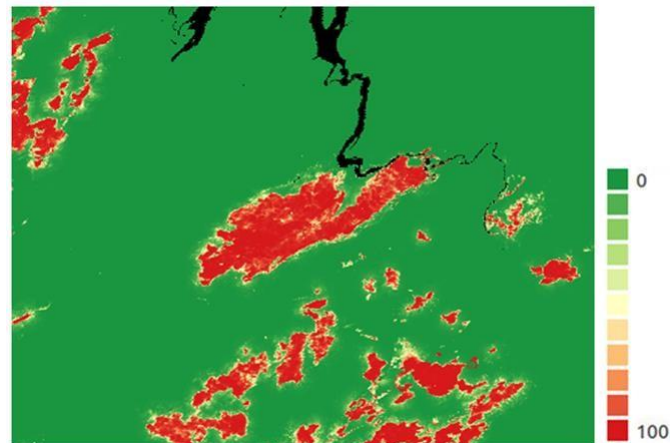
Figure 1. Uncertainty of an area of the tile h30v10 (Australia) for June 2008. The values represent the probability of each pixel being burned. Source: Lizundia-Loiola et al. 2018.

4.2 FireCCISFD20

The FireCCISFD20 product will be derived from the MSI sensor aboard two different satellites: Sentinel-2A and Sentinel-2B. Due to a spatial shift between S2A and S2B data, errors were observed to increase when using data from both satellites at the same time. For this reason, the algorithm will generate two independent BA products, each based on images from one satellite, which will be merged in a final step. Each intermediate BA product detects initial burned areas between two dates based on fixed thresholds and proximity to active fires. Then, statistics for MIRBI and NBR2 spectral indices are extracted from these initial BA, which are used to assign the final probability of burn of the whole image, from 0 to 100%. In this way a probability image is obtained for the image from every single date (Roteta et al., 2019).

Both BA products corresponding to S2A and S2B satellites are fused in the final FireCCISFD20 product. In a temporal series of $\{t_{0,A}, t_{1,B}, t_{2,A}, t_{3,B}, \ldots, t_n\}$ where every element corresponds to a date (with $_A$ and $_B$ standing for S2A and S2B dates), burned pixels in any S2A date ($t_{i,A}$) are assigned a 0% probability if they were not detected as burned in the last day of observation before $t_{i,A}$ ($t_{i-1,B}$) or in the first day of observation after $t_{i,A}$ ($t_{i+1,B}$) in the S2B product. In this way many commissions due to unmasked clouds and cloud shadows are reduced. Finally, the monthly product is created assigning to each pixel the date when the highest probability was observed; pixels for which no probability higher than 50% was observed are considered unburned and assigned a 0% probability in the monthly product.

4.3 FireCCIS310

This product refers to the BA derived from S3 SYN data. Due to the pre-processing problems of SYN data, we plan to produce two years of BA products (2019 and 2020). This implies that the expected validation dataset (2017-2019) will be restricted to a single year. We will use these data to generate the uncertainty characterization of the FireCCIS310 product. We will consider BA algorithm inputs and output over all validation areas to estimate the performance of the algorithm over a large variety of inputs. To reduce the dimensionality of that highly redundant data set and to drastically reduce the computational effort to compute uncertainties, a look up table (LUT) of representative spatiotemporal signal patterns can be derived from that data set. A reasonable number of distinct spatiotemporal patterns will be taken into account from the validation data set.

Given the representativeness of validation data, those should be sufficient to describe the full range of typical spatiotemporal patterns in the data.

For example, if the classification burned/unburned at a given pixel is characterized by its post-NIR value (X) and some statistics that quantifies the drop of NIR from a pre-time window to a post-time window (T), the spatiotemporal pattern is a vector $(X, T, X_1, T_1,..., X_n, T_n)$ where X and T describe the pixel that we want to classify and the rest of the pairs $(X_1, T_1,..., X_n, T_n)$ describe its spatial neighbours. In this case, n is the number of spatial neighbour pixels that are taken into account by the algorithm to determine if a pixel is burned or not. In that way, after running the algorithm for all the validation sites we can obtain similar information to what is shown in Table 2.

Table 2. Example of the matrix that can be obtained from an algorithm that uses two variables (X and T) and n neighbour pixels to classify the pixel i as burned(B)/unburned(UB).

	Spatiotemporal pattern							Classification	
	X_i	T_i	X_{i1}	T_{i1}	…	X_{in}	T_{in}	Validation	Algorithm
Pixel 1	X_1	T_1	X_{11}	T_{11}	…	X_{1n}	T_{1n}	B or UB	B or UB
Pixel 2	X_2	T_2	X_{21}	T_{21}	…	X_{2n}	T_{2n}	B or UB	B or UB
Pixel 3	X_3	T_3	X_{31}	T_{31}	…	X_{3n}	T_{3n}	B or UB	B or UB
Pixel 4	X_4	T_4	X_{41}	T_{41}	…	X_{4n}	T_{4n}	B or UB	B or UB
…	…	…	…	…	…	…	…	…	…
Pixel m	X_m	T_m	X_{m1}	T_{m1}	…	X_{mn}	T_{mn}	B or UB	B or UB

Those pixel-level spatiotemporal patterns can be grouped to create representative spatiotemporal patterns (P) based on a cluster analysis. Thus, instead of having m pixels, we can group them in S general spatiotemporal patterns $(P_1, P_2, …, P_S)$. Given that set of "representative patterns", the algorithm uncertainty can be estimated directly by comparing the algorithm's output with validation data. Using the BA algorithm outputs and the reference, one can estimate from all N cases that belong to the spatiotemporal pattern P, the 4 conditional probabilities. Uncertainty would be some function of those conditional probabilities that has to be defined.

The result will be a collection of representative patterns $(P_1, P_2,...)$, and associated "probabilities of burn detection" $(pb_1, pb_2,...)$ that will be saved in a LUT. To compute an uncertainty layer for the whole burned area product, each pixel has to be associated to its own representative pattern or to the closest representative pattern and labelled with the corresponding probability of burn.

Furthermore, the "black box" approach will allow propagating uncertainties using Monte Carlo methods, providing a sound alternative to tracing uncertainty through the algorithm. Given uncertainties in L1 products, Monte Carlo simulations can be performed to quantify the distribution D of those variables (X and T in the example above) that classify a pixel as burned/unburned. For S3, the error layer that is provided along with the reflectance in SYN (Section 3.3) will be used as a proxy of the input uncertainty. To limit computational requirements, this only needs to be done for combinations of those variables that occur in representative patterns. More specifically, for each representative pattern, the burn area algorithm is run over perturbed versions of that pattern, and outputs are compared with the LUT derived from validation data. This will allow quantifying the stability of the algorithm and its sensitivity to noise in L1 products. Fast Monte Carlo techniques for uncertainty propagation have been proposed, for instance, in Rochman et al. (2014), to overcome the drawback related to computational cost of this method.

The proposed method was developed by Professor Manuel Campagnolo (personal communication) of the University of Lisbon, who was involved in the previous Phases of the project. At the time of writing of this document we do not have any results to show due to the lack of availability of validation data for the year 2019. However, in the following version of the E3UB document results will be included. Besides, the idea is to analyse those probability of burn detections (pb) to build recommendations for the users about how to use this layer, e.g. specific thresholds to apply.

4.4   FireCCILT20 and FireCCIS1S2AF10

Both the FireCCILT20 and FireCCIS1S2AF10 products will be based on a model of deep learning, more specifically on a Convolutional Neural Network (CNN). Therefore, the same uncertainty characterisation and propagation framework can be developed in both cases, although they use different input datasets. Regarding the main input of the algorithm, AVH09 reflectance (Section 3.4) is used by FireCCILT20 while FireCCIS1S2AF10 make use of MSI and SAR data (Section 3.5 and 3.6, respectively). Land cover CCI (Section 3.7.3) is used by the two algorithms. Active fire information provided by MODIS (Section 3.7.1) and VIIRS (Section 3.7.2) is also used by the FireCCIS1S2AF10. Such remote sensing datasets are generally affected by noise and disturbances. Hence, instead of 'real' measurements ($\mathbf{v}$), what is actually fed to the model is a noisy version ($\mathbf{z}$) of such measurements (Loquercio et al., 2020).

The last layer of all CNN-based models is a Softmax layer (Krizhevsky et al., 2012), which is a logistic regression that normalizes an input value ($\mathbf{z}$) into probability values that ranges from 0 to 1:

$$P(\mathbf{z}_i) = \frac{e^{z_i}}{\Sigma_{j=1}^{n} e^{z_j}}$$

where $\mathbf{z}$ is the output of a fully-connected neural network of the class i (i.e. burned or unburned), e is the Euler's number and n is the number of classes (i.e. 2).

Softmax provides a discrete probability distribution over the burned and unburned classes. This probability value is based on the features extracted in the previous hidden layers of the model, which are affected by convolutional processes that consider the intrinsic uncertainty sources ($\mathbf{z}$). Due to the fact that only two classes (i.e., burned and unburned) were involved in the process, the probability of a given pixel to belong to the burned class (b) is inversely proportional to belong to the unburned one (u):

$$1 = P_b + P_u$$

Hence, such probability distribution may be used as a proxy to estimate the uncertainty. When low intrinsic errors of data are considered, the final probability of a pixel to belong to a given class is lower in comparison to when a high degree of interferences of errors exist (Rottmann & Schubert, 2019; Pascual et al., 2018). The Softmax layer may be considered, therefore, to characterise the uncertainty when mapping BA.

Other authors, however, pointed out that in CNN models the representation of the uncertainty could be poor (Jain et al., 2018). Since machine learning approaches are considered like "black boxes", there is no way to mathematically propagate the input uncertainty through the algorithm. Instead, to somehow improve this representativeness of uncertainty in the final probability, an approach that could be followed is to include the uncertainty layers of each predictive variable in the model. Ideally speaking, the uncertainty of all input variables should be provided in a pixel-based uncertainty layer.

When this is not the case, a preliminary uncertainty layer could be created based on the literature (Section 3.4). The aim of those "invented" uncertainties would not be to characterise the actual input uncertainty, but to create a layer that will serve to develop the propagation framework.

To illustrate the mentioned approach FireCCILT20 can be used as an example. In the case of this algorithm 12 predictive variables are included in the model to get the final burned probability. These variables represent the five previous monthly synthetic indices and the six posterior to the month for which burned area is going to be detected (Otón et al., 2019). To obtain the synthetic index first monthly composites of each AVH09 channel based on the maximum temperature are created. After that, two more steps are performed. First, monthly vegetation indices are computed based on the monthly composites and, second, the most significant variables are summed, after normalising each of them. In the first step, an uncertainty layer can be created in parallel directly transferring the pixel level uncertainty from the day selected by the composite. In the following two steps, uncertainty can be estimated through error propagation. Lewis et al. (2018) showed, using the example of NDVI vegetation index, how uncertainty could be estimated when ratio-difference transformations are applied. In the case of sums and subtractions, if it is assumed that errors are uncorrelated, the variance of the result is simply equal to the sum of the variances. For the ratio transformation, since it is not possible to directly apply linear propagation, it is common to approximate this by linear terms using a Taylor expansion instead. Mathematical expressions can be found in Lewis et al. (2018). The result of all this process would be an uncertainty layer per each monthly synthetic index that could be used as predictive variables, making a total of 24.

The problem with this approach is that it cannot be applied if an actual and proper uncertainty characterisation of the input datasets is not available. In the case of the FireCCIS310 (Section 4.3), for example, the uncertainty characterisation is independent to the BA detection and, therefore, a proxy uncertainty can be used to develop the propagation framework. However, when the uncertainty is included as predictive variable the results can be artificially altered. Therefore, the only option is to consider that the probability of burn given by the CNN correctly characterises the uncertainty, although no input uncertainty was included in the model.

5 Uncertainty characterisation at grid scale

The uncertainty aggregation at 0.25° grid product will be carried out following the approach developed within the previous phase by University College London that is described in Section 4 of Lewis et al., (2018). It can be easily applied also in the current project since it uses the probability of burn generated by the previously mentioned algorithms as input to propagate the uncertainty. This is a number between 0 (absolute certainty that the pixel did not burn in the temporal interval considered) to 1 (absolute certainty that the pixel did burn in the temporal interval considered).

From the point of view of the ESA Fire_cci pixel-level product, there are two layers which are relevant: the date of first detection, and the confidence level. Generally speaking, the burned area inside a Climate Model Grid (CMG) cell can be determined as the sum of pixels where the first date of detection is between 0 and 366 (both inclusive), multiplied by the area of the pixel. This is intuitive and in line with previous estimates. However, if the confidence layer is interpreted as a probability of burn, p_b, (and in consequence, a probability of not being burned of $1 - p_b$), then this information would need to be scaled up to the CMG, as a form of standard error. There are two common definitions relating to

standard error (Weisstein, 2017): (i) the square root of the estimated error variance (standard deviation); (ii) the standard error of a sample of size n is the sample standard deviation divided by $\sqrt{n}$. There is a need to consider then which would be appropriate in this context.

The sample variance σ^2 of a sample set of size n is given by:

$$\sigma^2 = \frac{1}{n}\sum_{i=1}^{n}(y_i - \bar{y})^2$$

where y_i is sample i and $\bar{y}$ is the sample mean, given by

$$\bar{y} = \frac{1}{n}\sum_{i=1}^{n}y_i$$

The sample terms $\bar{y}$ and σ^2 are random variables, and the expected value of the variance $\hat{\sigma}^2$ is given by

$$\hat{\sigma}^2 = \frac{n}{n-1}\sigma^2$$

Often, σ^2 is the biased sample variance and $\hat{\sigma}^2$ is the unbiased sample variance. Going back to the definitions of standard error, it can be said that the first definition $\hat{\sigma}_1$ (square root of the estimated error variance) is thus

$$\hat{\sigma}_1 = \frac{n}{n-1}\sigma$$

where σ is the sample standard deviation. Using the second definition (sample standard deviation divided by $\sqrt{n}$) we have that

$$\hat{\sigma}_2 = \frac{1}{\sqrt{n}}\sigma$$

The first definition is more consistent with many uses of standard error in the physical sciences, where it takes the role of an unbiased estimate of the standard deviation of a distribution. If the distribution is assumed normal and y is continuous (or effectively continuous if n is large), then the estimate of the mean ($\bar{y}$) and standard deviation (σ_1) fully define the Probability Distribution Function (PDF) for BA.

The second definition is more directly related to the uncertainty of the mean and is used in the definition of probable error. The standard error of the mean is given by σ_2. So, with more samples (greater n) we can better estimate the mean of the distribution.

In the light of this, we will use

$$\hat{\sigma} = \frac{1}{\sqrt{n-1}}\sum_{i=1}^{n}(y_i - \bar{y})^2$$

which is a unbiased estimate of the likely variability in burned area.

Assuming that each pixel has an independent probability of burn p_b, which can be different for every pixel, then the sum of these independent probabilities is given by a Poisson Binomial distribution. This distribution is only defined over positive integer numbers, and has first and second order statistics given by

$$\overline{N_b} = \sum_{i=1}^{N_p} p_{b,i}$$

$$\sigma_b^2 = \sum_{i=1}^{N_p} p_{b,i}(1 - p_{b,i})$$

In Figure 2, the full PDF derived from a set of samples each characterised by a different p_b is shown. We calculate the PDF as a Poisson binomial, and also calculate the mean and variance using the equations above, and plot the normal approximation to the PDF. For a large number of samples, the skewness of the PDF is very low, and the PDF is acceptably approximated by a Gaussian distribution. This is of importance, as it means that one can parametrize the full PDF of BA using only the mean and the "standard error" (defined as the standard deviation in the discussion above), and in accordance to the product specification.
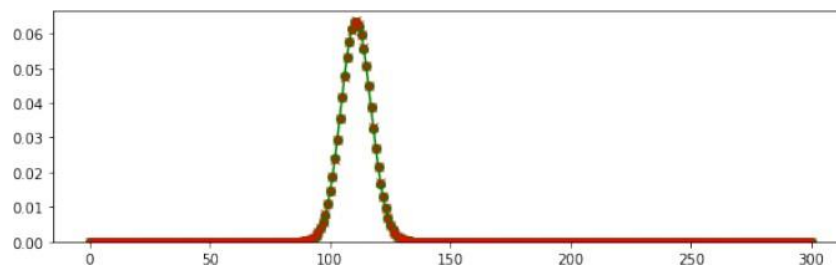
Figure 2. The Poisson binomial PDF (green line) derived from a simulated set of independent samples (300, 100 with probabilities between 0.7 and 0.9, 100 with probabilities between 0.2-0.3 and 100 with probabilities between 0-0.1). A Gaussian approximation (red line) derived from calculating the mean (~110) and standard deviation (~39) is also shown. Skewness was ~0.01. Source: Lewis et al. 2018.

6 References

ACRI-ST IPF Team (2017). Product Data Format Specification - OLCI Level 1 Products, version 2.2. Mission Performance Centre.

ACRI-ST IPF Team (2018). Product Data Format Specification - SLSTR Level 1 Products, version 2.7. Mission Performance Centre.

Ackerman, S., Frey, R., Strabala, K., Liu, Y., Gumley, L., Baum, B., & Menzel, P. (2010). Discriminating clear-sky from cloud with MODIS algorithm theoretical basis document (MOD35). Available at: https://modis.gsfc.nasa.gov/data/atbd/atbd_mod06.pdf

Anfinsen, S. N., Doulgeris, A. P., & Eltoft, T. (2009). Estimation of the equivalent number of looks in polarimetric synthetic aperture radar imagery. IEEE Transactions on Geoscience and Remote Sensing, 47(11), 3795-3809.

Belenguer-Plomer, M. A., Tanase, M. A., Fernandez-Carrillo, A., & Chuvieco, E. (2018). Temporal backscattering coefficient decorrelation in burned areas. In Active and Passive Microwave Remote Sensing for Environmental Monitoring II, p. 107880T. International Society for Optics and Photonics.

Belenguer-Plomer, M. A., Tanase, M. A., Fernandez-Carrillo, A., & Chuvieco, E. (2019). Burned area detection and mapping using Sentinel-1 backscatter coefficient and thermal anomalies. Remote Sensing of Environment, 233, 111345.

Brennan, J., Gómez-Dans, J.L., Disney, M., & Lewis, P. (2019). Theoretical uncertainties for global satellite-derived burned area estimates. Biogeosciences, 16, 3147-3164

Bulgin, C.E., Embury, O., & Merchant, C.J. (2016). Sampling uncertainty in gridded sea surface temperature products and Advanced Very High Resolution Radiometer (AVHRR) Global Area Coverage (GAC) data. Remote Sensing Of Environment, 177, 287-294

Burnicki, A.C. (2011). Modeling the Probability of Misclassification in a Map of Land Cover Change. Photogrammetric Engineering & Remote Sensing, 77, 39-49.

Chuvieco, E., Pettinari, M.L., Heil, A., & Storm, T. (2017) ESA CCI ECV Fire Disturbance: D1.2 Product Specification Document, version 6.3. Available at: https://www.esa-fire-cci.org/documents

Crosetto, M., Moreno, J.A., & Crippa, B. (2001). Uncertainty propagation in models driven by remotely sensed data. Remote Sensing of Environment, 76, 373-385.

Crosetto, M., & Tarantola, S. (2001). Uncertainty and sensitivity analysis: tools for GIS-based model implementation. International Journal of Geographical Information Systems, 15, 415-437.

El Saleous, N., Vermote, E., Justice, C., Townshend, J., Tucker, C., & Goward, S. (2000). Improvements in the global biospheric record from the Advanced Very High Resolution Radiometer (AVHRR). International Journal of Remote Sensing, 21, 1251-1277

ESA, 2017a. Land cover CCI product user guide version 3. Tech. Rep Available at: https://www.esa-landcover-cci.org/?q=webfm_send/123.

ESA, 2017b. Land cover CCI algorithm theoretical basis document, Part III: classification year 2, version 1.2. Tech. Rep Available at: https://www.esa-landcover-cci.org/?q=webfm_send/139

EUMESAT (2011). AVHRR Level 1b Product Guide. In: EUM/OPS-EPS/MAN/04/0029 Issue: v3A Date: 21 Jan 2011. Available from: https://www.eumetsat.int/website/wcm/idc/idcplg?IdcService=GET_FILE&dDocName=PDF_AVHRR_L1B_PRODUCT_GUIDE&RevisionSelectionMethod=LatestReleased&Rendition=Web

Etxaluze, M., & Smith, D. (2019). Sentinel-3 SLSTR Uncertainties in Level-1 Products Algorithm and Theoretical Basis Document. RAL Space for Copernicus.

Giglio, L., Loboda, T., Roy, D.P., Quayle, B., & Justice, C.O. (2009). An active-fire based burned area mapping algorithm for the MODIS sensor. Remote Sensing of Environment, 113, 408-420.

Giglio, L., Randerson, J., T., van der Werf, G.R., Kasibhatla, P., Collatz, G.J., Morton, D.C., & Defries, R. (2010). Assessing variability and long-term trends in burned area by merging multiple satellite fire products. Biogeosciences, 7, 1171-1186.

Giglio, L., Schroeder, W., & Justice, C. O. (2016). The collection 6 MODIS active fire detection algorithm and fire products. Remote Sensing of Environment, 178, 31-41.

Giglio, L., Boschetti, L., Roy, D.P., Humber, M.L., & Justice, C.O., (2018a). The Collection 6 MODIS burned area mapping algorithm and product. Remote Sensing of Environment. 217, 72–85.

Giglio, L., Schroeder, W., Hall, J. V., & Justice, C. O. (2018b). MODIS Collection 6 Active Fire Product User's Guide, Revision B. NASA.

Goncalves, J., & Fernandes, J. C. (2005). Assessment of SRTM-3 DEM in Portugal with topographic map data. In Proceedings of the EARSeL Workshop 3D-Remote Sensing, 10-11.

Gorroño, J., Fomferra, N., Peters, M., Gascon, F., Underwood, C.I., Fox, N.P., Kirches, G., & Brockmann, C. (2017). A radiometric uncertainty tool for the Sentinel 2 mission, Remote Sensing, 9, 178.

GUM 2008 JCGM 100:2008 Guide to the expression of Uncertainty in Measurement (JCGM) p 100 (www.bipm.org)

GUM-101 2008 JCGM 101:2008, Evaluation of measurement data — Supplement 1 to the "Guide to the expression of uncertainty in measurement" — Propagation of distributions using a Monte Carlo method (www.bipm.org)

Holben, B.N., Kaufman, Y.J., & Kendall, J.D. (1990). NOAA-11 AVHRR visible and near-IR inflight calibration. International Journal of Remote Sensing, 11, 1511-1519.

Hunt, S., & Nieke, J. (2016). A Radiometric Uncertainty Tool for OLCI. In, Proceedings Living Planet Symposium, 9-13.

Jain, A., Fandango, A., & Kapoor, A. (2018). TensorFlow Machine Learning Projects: Build 13 real-world projects with advanced numerical computations using the Python ecosystem. Packt Publishing Ltd.

Kalogirou, V., Ferrazzoli, P., Della Vecchia, A., & Foumelis, M. (2014). On the SAR backscatter of burned forests: A model-based study in C-band, over burned pine canopies. IEEE Transactions on Geoscience and Remote Sensing, 52(10), 6205-6215.

Krizhevsky, A., Sutskever, I., & Hinton, G. E. (2012). Imagenet classification with deep convolutional neural networks. In Advances in neural information processing systems (pp. 1097-1105).

Kurum, M. (2015). C-band SAR backscatter evaluation of 2008 Gallipoli forest fire. IEEE Geoscience and Remote Sensing Letters, 12(5), 1091-1095.

Lewis, P., Gomez Dans, J., Brennan, J., & Chernetskiy, M. (2018) ESA CCI ECV Fire Disturbance: D3.1. Comprehensive Error Characterization Report, version 2.0. Available at: https://www.esa-fire-cci.org/documents

Lizundia-Loiola, J., Otón, G., Ramo, R., & Chuvieco, E. (2020). A spatio-temporal active-fire clustering approach for global burned area mapping at 250 m from MODIS data. Remote Sensing of Environment, 236, 111493.

Lizundia-Loiola, J., Pettinari, M.L., Chuvieco, E., Storm, T., & Gómez-Dans, J. (2018) ESA CCI ECV Fire Disturbance: D2.1.3 Algorithm Theoretical Basis Document-MODIS, version 2.0. Available at: https://www.esa-fire-cci.org/documents

Loquercio, A., Segu, M., & Scaramuzza, D. (2020). A general framework for uncertainty estimation in deep learning. IEEE Robotics and Automation Letters, 5(2), 3153-3160.

Main-Knorn, M., Pflug, B., Louis, J., Debaecker, V., Müller-Wilm, U., & Gascon, F. (2017). Sen2Cor for Sentinel-2. In Image and Signal Processing for Remote Sensing XXIII p. 1042704. International Society for Optics and Photonics.

Merchant, C.J., Paul, F., Popp, T., Ablain, M., Bontemps, S., Defourny, P., Hollmann, R., Lavergne, T., Laeng, A., & de Leeuw, G. (2017). Uncertainty information in climate data records from Earth observation. Earth System Science Data, 9, 511–527.

Mittaz, J., Merchant, C.J., & Woolliams, E.R. (2019). Applying principles of metrology to historical Earth observations from satellites. Metrologia, 56, 032002.

North, P. & Heckel, A. (2010) Sentinel-3 Optical products and algorithm definition. SYN Algorithm Theoretical Basis Document.

Otón, G., Ramo, R., Lizundia-Loiola, J., & Chuvieco, E. (2019). Global Detection of Long-Term (1982–2017) Burned Area with AVHRR-LTDR Data. Remote Sensing, 11, 2079.

Padilla, M. & Chuvieco, E. (2014) ESA CCI ECV Fire Disturbance: D1.2.3 Comprehensive Error Characterisation Report, version 2.1. Available at: https://www.esa-fire-cci.org/documents

Pascual, G., Seguí, S., & Vitrià, J. (2018). Uncertainty Gated Network for Land Cover Segmentation. In CVPR Workshops, pp. 276-279.

Pettinari, M.L., Chuvieco, E., Lizundia-Loiola, J., & Tanase, M. (2019) ESA CCI ECV Fire Disturbance: D1.2 Algorithm Development Plan, version 1.1. Available at: https://www.esa-fire-cci.org/documents

Pedelty, J., Devadiga, S., Masuoka, E., Brown, M., Pinzon, J., Tucker, C., Vermote, E., Prince, S., Nagol, J., Justice, C., Roy, D., Ju, J., Schaaf, C., Liu, J., Privette, J., & Pinheiro, A. (2007). Generating a long-term land data record from the AVHRR and MODIS instruments. In, Geoscience and Remote Sensing Symposium, 2007. IGARSS 2007. IEEE International, 1021-1025.

Quegan, S., & Yu, J. J. (2001). Filtering of multichannel SAR images. IEEE Transactions on Geoscience and Remote Sensing, 39(11), 2373-2379.

Robel, J., Graumann, A., Kidwell, K., Aleman, R., Ruff, I., Muckle, B., & Kleespies, T. (2014). NOAA KLM User's Guide with NOAA-N, N Prime, and MetOp Supplements. National Oceanic and Atmospheric Administration, Washington.–2530 p. Available at: https://www1.ncdc.noaa.gov/pub/data/satellite/publications/podguides/N-15_thru_N-9/pdf/0.0_NOAA_KLM_Users_Guide.pdf

Rochman, D., van der Marck, S.C., Koning, A.J., Sjöstrand, H. & Zwermann, W. (2014). Uncertainty Propagation with Fast Monte Carlo Techniques, Nuclear Data Sheets, 118, 367-369.

Roteta, E., Bastarrika, A., Padilla, M., Storm, T., & Chuvieco, E. (2019). Development of a Sentinel-2 burned area algorithm: Generation of a small fire database for sub-Saharan Africa. Remote sensing of environment, 222, 1-17.

Rottmann, M., & Schubert, M. (2019). Uncertainty measures and prediction quality rating for the semantic segmentation of nested multi resolution street scene images. In: Proceedings of the IEEE Conference on Computer Vision and Pattern Recognition Workshops (9 pp.). Available at: http://openaccess.thecvf.com/content_CVPRW_2019/papers/SAIAD/Rottmann_Uncertainty_Measures_and_Prediction_Quality_Rating_for_the_Semantic_Segmentation_CVPRW_2019_paper.pdf

S3 Team (2011). Level 1 Algorithms Theoretical baseline Document – Part 2: optical products [SY-24] Level 1C ATBD. Thales Alenia Space.

Sayer, A.M, Govaerts, Y., Kolmonen, P., Lipponen, A., Luffarelli, M., Mielonen, T., Patadia, F., Popp, T., Povey, A.C., Stebel, K., Witek, M.L. (2020). A review and framework for the evaluation of pixel-level uncertainty estimates in satellite aerosol remote sensing. Atmospheric Measurement Techniques 13, 373-404.

Schroeder, W., Oliva, P., Giglio, L., & Csiszar, I. A. (2014). The New VIIRS 375m active fire detection data product: algorithm description and initial assessment, Remote Sensing of Environment, 143, 85-96.

Schwerdt, M., Schmidt, K., Tous Ramon, N., Klenk, P., Yague-Martinez, N., Prats-Iraola, P., Zink, M., & Geudtner, D. (2017). Independent system calibration of Sentinel-1B. Remote Sensing, 9(6), 511.

Smith, J.H., Stehman, S.V., Wickham, J.D., & Yang, L. (2003). Effects of landscape characteristics on land-cover class accuracy. Remote Sensing of Environment, 84, 342-349.

Stoffelen, A. (1998). Toward the true near-surface wind speed: Error modelling and calibration using triple collocation, J. Geophys. Res.- Oceans, 103, 7755–7766.

Trishchenko, A.P., Fedosejevs, G., Li, Z., & Cihlar, J. (2002). Trends and uncertainties in thermal calibration of AVHRR radiometers onboard NOAA-9 to NOAA-16. Journal of Geophysical Research: Atmospheres, 107 (D24), 4788.

Uprety, S., & Cao, C. (2011). Using the Dome C site to characterize AVHRR near-infrared channel for consistent radiometric calibration. Earth Observing Systems XVI, 81531Y: International Society for optics and Photonics.

van Oort, P.A.J., Bregt, A.K., de Bruin, S., de Wit, A.J.W., & Stein, A. (2011). Spatial variability in classification accuracy of agricultural crops in the Dutch national land-cover database. International Journal of Geographical Information Science, 18, 611-626.

Vermote, E. F., & Saleous, N. (2006). Operational atmospheric correction of MODIS visible to middle infrared land surface data in the case of an infinite Lambertian target. In Earth science satellite remote sensing (pp. 123-153). Springer, Berlin, Heidelberg.

Vermote, E. F., & Kotchenova, S. (2008). Atmospheric correction for the monitoring of land surfaces. Journal of Geophysical Research: Atmospheres, 113(D23).

Vermote, E., Roger, J., & Ray, J. (2015). MODIS Surface Reflectance User's Guide-Collection 6. Tech. Rep. Version 1.4, NASA GSFC Terrestrial Information Systems Laboratory, MODIS Land Surface Reflectance Science Computing Facility: Greenbelt, USA.

Weisstein, Eric W (2017). "Standard Error." From MathWorld--A Wolfram Web Resource. http://mathworld.wolfram.com/StandardError.html

Xiong, J., Toller, G., Sun, J., Wenny, B., Angal, A., & Barnes, W. (2013). MODIS level 1B algorithm theoretical basis document, version 4. NASA MODIS characterization support team, Washington, DC.

Annex 1 Acronyms and abbreviations

AC	Atmospheric Correction
ADC	Analog-to-Digital Converter
ADF	Auxiliary Data Files
ADP	Algorithm Development Plan
AERONET	Aerosol Robotic Network
AOD	Aerosol Optical Depth
AOT	Atmospheric Optical Thickness
ASCII	American Standard Code for Information Interchange
ATBD	Algorithm Theoretical Basis Document
AVH09	AVHRR Surface Reflectance Product of Land Long Term Data Record project
AVHRR	Advanced Very High Resolution Radiometer
BA	Burned area
BC	Brockmann Consult GmbH
BOA	Bottom-of-Atmosphere
BRDF	Bidirectional reflectance distribution function
BT	Brightness Temperature
C3S	Copernicus Climate Change Service
CCD	Charge-Coupled Device
CCI	Climate Change Initiative
CMG	Climate Model Grid
CNN	Convolutional Neural Networks
CRG	Climate Research Group
dB	decibel
E3UB	End-to-End ECV Uncertainty Budget
ECV	Essential Climate Variable
ENL	Equivalent Number of Looks
Envisat	Environmental Satellite
EO	Earth Observation
ERS	European Remote Sensing satellite
ESA	European Space Agency
EUMESAT	European Organisation for the Exploitation of Meteorological Satellites
EV	Earth View
FireCCI51	Fire_cci MODIS version 5.1
FireCCILT10	Fire_cci AVHRR-LTDR version 1.0
FireCCILT20	Fire_cci AVHRR-LTDR version 2.0
FireCCIS1S2AF10	Fire_cci Sentinel-1 & Sentinel-2 test sites in AFrica version 1.0
FireCCIS310	Fire_cci Sentinel-3 version 1.0
FireCCISFD20	Fire_cci Small Fire Database version 2.0
FIRMS	Fire Information for Resource Management System
GAC	Global Area Coverage
GFED	Global Fire Emissions Database

GRD	Ground Range Detected
GUM	Guide to the Expression of Uncertainty in Measurement
IFOV	Instantaneous Field of View
IR	Infrared
ISP	Instrument Source Packet
IW	Interpherometric Wide
JCGM	Joint Committee for Guides in Metrology
JPSS	Joint Polar Satellite System
K	Kelvin
L0	Level 0
L1	Level 1
L2	Level 2
L3	Level 3
L4	Level 4
LC	Land Cover
LTDR	Long Term Data Record
LUT	Look-Up-table
MapnoiS3	Sentinel-3 Noise Mapping python tool
MCD14ML	MODIS Global Monthly Fire Location Product
MCD64	MODIS Collection 5 and 6 Burned Area product using the Giglio et al. (2009) and Giglio et al. (2018a) algorithm, respectively
MCST	MODIS Characterization and Support Team
MIRBI	Mid-Infrared Burn Index
MOD09	MODIS Terra Surface Reflectance 5-minute L2 Swath
MOD09GA	MODIS Terra Surface Reflectance Daily L2G Global 500 m and 1 km
MOD09GQ	MODIS Terra Surface Reflectance Daily L2G Global 250 m
MOD14/MYD14	MODIS Terra/Aqua active fire and other thermal anomalies product
MOD35	MODIS Cloud Mask product
MODIS	Moderate Resolution Imaging Spectroradiometer
MODLAND	MODIS Land Team
MSI	MultiSpectral Instrument
NASA	National Aeronautics and Space Administration
NBR2	Normalized Burn Ratio 2
NetCDF	Network Common Data Form
NIR	Near-InfraRed
NOAA	National Oceanic and Atmosphere Administration
NPP	National Polar-orbiting Partnership
NRT	Near Real Time
NTC	Non-Time Critical
OLCI	Ocean and Land Colour Instrument
OZA	OLCI Zenith Angle
PDF	Probability Distribution Function
PDGS	Payload Data Ground Segment
PRT	Platinum Resistance Thermometer

PSD	product Specification Document
PUG	Product user Guide
QA	Quality Assurance
QI	Quality Indicators
S1	Sentinel-1
S2	Sentinel-2
S2-RUT	Sentinel-2 radiometric uncertainty Tool
S3	Sentinel-3
SAR	Synthetic Aperture Radar
SCM	Scene Classification Map
Sen2Cor	Sentinel 2 Level 2A product generation and formatting processor
SLC	Single Look Complex
SLSTR	Sea and land Surface Temperature Radiometer
SNAP	Sentinels Application Platform
SRF	Spectral Response Function
SRTM DEM	Shuttle Radar Topography Mission Digital Elevation Model
SST	Sea Surface Temperature
Suomi-NPP	Suomi National Polar-orbiting Partnership satellite
SWIR	Short-Wave InfraRed
SY_1_MISR	Internal Synergy Level 1 product
SY_2_SYN	Synergy Surface Directional Reflectance product
SYN	Synergy
TC	Triple Collocation
TCI	True Color Image
TOA	Top-of-Atmosphere
TOPSAR	Terrain Observation with Progressive Scans SAR
VIIRS	Visible Infrared Imaging Radiometer Suite
VISCAL	Visible Calibration unit
VNP14ML	VIIRS Global Monthly Fire Location Product at 750 m
VNPIMG14ML	VIIRS Global Monthly Fire Location Product at 375 m
WV	Water Vapour